THE JOURNAL OF PHYSICAL CHEMISTRY C
A JOURNAL OF THE AMERICAN CHEMICAL SOCIETY

pubs.acs.org/JPCC

Article

Creating Functional Oxynitride–Silicon Interfaces and $SrNbO_2N$ Thin Films for Photoelectrochemical Applications

Shinjae Hwang, Spencer H. Porter, Mengjun Li, Ryan Thorpe, Anders B. Laursen, Hengfei Gu, Ahmad Safari, Martha Greenblatt,* Eric Garfunkel,* and G. Charles Dismukes*

Cite This: *J. Phys. Chem. C* 2022, 126, 5970–5979

Read Online

ACCESS | Metrics & More | Article Recommendations | Supporting Information

ABSTRACT: The effect of absorption length, carrier diffusion length, and surface area of an oxynitride photoabsorber on the photoelectrochemical performance is investigated, and how to best fabricate optical-quality thin films of band gap-tunable oxynitrides is also discussed. We targeted the stoichiometric compound $SrNbO_2N$ as an optimal wide-band-gap photoabsorber (1.9 eV) for use with silicon (1.1 eV) in a tandem structure photoelectrochemical cell. The preparation of perovskite oxynitrides at high temperatures as isolated powders is often straightforward, but it is difficult to integrate them as thin films in tandem junction devices with low-temperature materials. Here, we develop the first method to prepare optical-quality $SrNbO_2N$ thin films of tunable thickness and roughness on a single-crystal silicon substrate. To achieve this, an interfacial layer of ultrathin tantalum nitride (TaN) was used as a barrier to reduce the interdiffusion of silicon and oxygen during oxynitride synthesis. We prepared $SrNbO_2N$ films of varying thicknesses (20–440 nm) on doped n^+-Si(100) surfaces. The roughness factor (0.14–21) was scaled with thickness. The intrinsic photoelectrochemical activity of these devices was evaluated using a low-barrier sacrificial electron donor. Photocurrent density and photovoltage revealed a significant (and nonlinear) dependence on film thickness and roughness. Absorption length, carrier diffusion length, and surface area were each found to play key roles, and it is imperative to balance these properties to achieve optimal device performance.

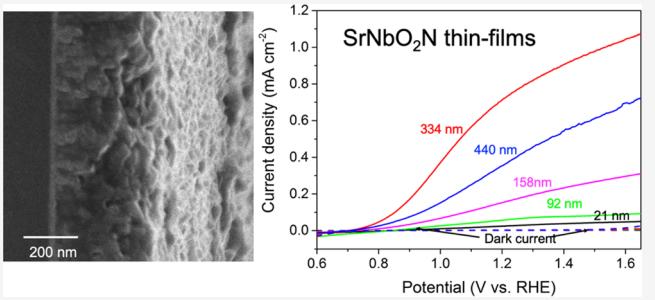

INTRODUCTION

Energy storage in chemical bonds offers higher capacity than that in batteries and is safe, has long-term stability, and allows conventional gas transport. H_2 derived from solar water splitting devices is a preferred renewable energy carrier as it can be directly converted back to electricity via fuel cells.[1] Current photoelectrochemical (PEC) devices for water electrolysis suffer from one or more of the following pitfalls: low stability, high cost, and/or low efficiency. Several PEC devices have been investigated to address these problems, including metal-oxide semiconductors due to their low cost, nontoxicity, and elemental abundance. However, even though large improvements have been made over several years, they still suffer from limited spectral coverage (large band gaps >2.4 eV) and short carrier diffusion lengths (recombination) that prevent this class of materials from achieving >10% solar-to-hydrogen (STH) efficiency.[2−5]

Perovskite oxynitrides $AB(O,N)_3$ (A = Ca, Sr, Ba, and La; B = Ti, Ta, and Nb) have promising physical properties that allow them to serve as visible-light-driven photoanodes for water oxidation, including high dielectric constant, narrower/tunable band gaps, and appropriate band edge positions. Tunability is achieved by employing different combinations of A and B cations as well as O/N ratios.[6−8] This class of materials has band gaps (1.7–2.3 eV)[9−13] that are suitable for use as a top junction in tandem with a low band gap semiconductor.

$SrNbO_2N$ is a perovskite oxynitride that has a nearly ideal band gap (1.8–1.9 eV) with optimal absorption (650–700 nm) for pairing with a lower band gap photoabsorber such as silicon.[14]

The photocatalytic activity of $SrNbO_2N$ as a powder has been reported, and electrophoretic deposition[15] or particle transfer[10,16] methods on conductive electrodes have been employed to produce porous and thick films of $SrNbO_2N$ from presynthesized microparticles.[10]

Photocatalytic activity and long-wavelength absorption up to 700 nm have been demonstrated,[10] but these attempts have often resulted in unstable films,[14] with limited control over the film thickness and film roughness, both of which are critical to optimizing light attenuation and carrier diffusion in the

Received: November 29, 2021
Revised: February 22, 2022
Published: March 28, 2022

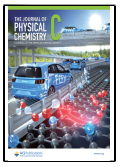

semiconductors.[5,17,18] Thin-film fabrication methods allow control of these variables and are well suited for integration with bottom junction photoabsorbers (e.g., Si). Unfortunately, because high temperatures are needed for ammonolysis to convert oxide precursor films into an oxynitride, it has been extremely challenging to prepare a $SrNbO_2N$ film without intermixing at the $SrNbO_2N$/conductive or light absorber interface.[19] Kawashima et al.[14] demonstrated the formation of a crystalline film of what is nominally $SrNbO_2N$ on an Nb substrate, but they observed a significant reduction of Nb^{5+} to Nb^{4+}, resulting in parasitic absorption in the near-IR and poorer PEC performance. A recent study from Kikuchi et al.[20] demonstrated the one-step epitaxial growth of $SrNbO_2N$ on $SrTiO_3$ by RF reactive sputtering, achieving an indirect band gap of 1.81 eV. However, this material had lower carrier mobility due to the trapping of electrons at grain boundaries.[20] These and other researchers have not fully investigated the effect of key performance variables such as film thickness and their impact on photoelectrochemical properties in oxynitride materials.

Cubic-TaN has been widely used as a diffusion barrier for metals on Si under high-temperature processing conditions.[21,22] Compared to common diffusion barriers such as TiN,[23,24] c-TaN has higher density and low formation energy,[22,25] making these materials superior for the prevention of interdiffusion of metal and metal oxide. In addition, it has the metallic properties needed for a low impedance interface. In this work, we fabricated $SrNbO_2N$/TaN on Si substrates that have the potential to be used as a tandem photoabsorber structure. An ultrathin film of TaN introduced between the strontium niobium oxide thin film and the crystalline Si substrate served as an effective interfacial diffusion barrier during ammonolysis to form $SrNbO_2N$. Diffraction, elemental, and chemical state analysis confirm the pure-phase $SrNbO_2N$ without commonly found reduced niobium (Nb^{4+}) for Nb-based oxynitrides.[26] Herein, we apply these approaches for the first time to prepare optical-quality thin films of $SrNbO_2N$ for application as a photoanode.

EXPERIMENTAL SECTION

Materials. $Sr(NO_3)_2$ (Sigma, 99.99%), $NbCl_5$ (Alfa, 99.9%), citric acid (Sigma, 99%), TaN target (Kurt J. Lesker, 99.5%), n^+-Si(100) (University wafer, as-doped, 0.005 Ω/cm), and 200 proof ethanol (Fisher Scientific, 100%) were used as received.

Preparation of the $SrNbO_2N$/TaN Thin Films on Si and Quartz. n^+-Si(100) substrates were cleaned with acetone, ethanol, and deionized water, followed by immersion for 5 min in a buffered oxide etch (BOE) solution and 6:1 vol NH_4F/HF, prior to introduction into a pulsed laser deposition (PLD) vacuum chamber. Pulsed laser ablation of TaN and $Sr_2Nb_2O_7$ targets was carried out using a KrF excimer laser COMPex 205 (λ = 248 nm, d = 7 cm, 10 Hz, 2.5−5 J/cm^2; Coherent).[23] The chamber base pressure was kept at 5−7 × 10^{-4} Pa. TaN deposition was carried out using the TaN target under a partial pressure of ultrahigh purity nitrogen (P_{N_2}: 6.7 Pa, 700 °C). Except for the X-ray diffraction (XRD) study, the thickness of TaN was maintained in the range of 5−10 nm. $Sr_2Nb_2O_7$ target was ablated at a P_{N_2} of 26.7 Pa at 700 °C right after the TaN deposition. Only the ablation time was varied for different thicknesses of the oxide films. The films were converted into the oxynitride, $SrNbO_2N$, by postannealing in a tube furnace (NH_3 atmosphere at 250 mL/min, 840 °C dwell for 1−2 h, and 20 °C/min ramp-up). The $Sr_2Nb_2O_7$ target for PLD was prepared by uniaxially pressing (105 MPa) $Sr_2Nb_2O_7$ powder and then sintering at 1400 °C for 15 h with a 10 °C/min ramp and cool. Details of the $Sr_2Nb_2O_7$ powder synthesis are reported elsewhere.[19] For optical measurements, $SrNbO_2N$/TaN layers were deposited on a quartz substrate (Advalue technology) as noted above, except that the ammonolysis annealing was limited to 820 °C to prevent the atomic diffusion of SiO_2.

Physical/Chemical Characterizations. X-ray diffraction (XRD) was carried out on a Bruker D8 ADVANCE (Cu Kα1, 0.02° step size, 15−20 s dwell time). Rutherford backscattering spectrometry (RBS) was performed using the Rutgers 1.7 MV General Ionex Tandetron. The incident beam was 2.0 MeV He ions, and recoiled He ions were measured with a standard ORTEC Si surface barrier detector (scattering angle (δ) = 163°, energy resolution ∼17 keV). The RBS data were analyzed using the SIMNRA program.[27] Helium ion microscopy (HIM) was carried out in an Orion Plus Helium Ion Microscope (ZEISS). Operating acceleration voltage and ion beam current were set at 30 kV and 1 pA, respectively. For X-ray photoelectron spectroscopy (XPS) measurements, a Thermo K-Alpha spectrometer was used with charge compensation; spectra were calibrated against adventitious carbon (284.8 eV). UV−vis diffuse reflectance was carried out on $SrNbO_2N$/TaN/quartz and TaN/quartz systems using a 300 W Xe arc lamp (Oriel) with an integrating sphere (Si photonics) equipped with a Flame S detector (Ocean Optics). UV−vis transmittance measurements were carried out with an HP diode array spectrometer.

Photoelectrochemical Measurements. Photoelectrochemical oxidation of ferrocyanide was measured in a 1 × 5 cm^2 glass cuvette cell (FireflySci, Inc.) in 0.1 M $K_4[Fe(CN)_6]$/1 mM $K_3[Fe(CN)_6]$ with 0.1 M KOH (pH 13.0) using a Bio-Logic potentiostat (VSP-300). The working electrodes were illuminated by simulated 1.5 AM G generated by a 300 W Xe arc lamp (ORIEL), which was calibrated against a $GaInP_2$ reference solar cell (NREL). The distance between the glass window and the working electrode was kept at 1 mm. A Pt wire (BASi) was used for the counter electrode, and a mercury/mercury oxide (1 M NaOH) reference electrode (CH Instrument) was used. The reference electrode potential was calibrated against the reversible hydrogen electrode (RHE, freshly cleaned Pt electrode at 1 atm H_2) before each measurement.

Incident Photon-to-Current Efficiency (IPCE) Measurements. IPCE measurements were performed using monochromated light from a 300 W Xe arc lamp (ORIEL) with the same 3-electrode setup for photoelectrochemical measurements. The wavelength of light was selected with a monochromator (ORIEL) in the range of 400−700 nm at 50 nm intervals. The measurements were performed from low to high wavelength. The working electrode potential was held at 1.23 V vs RHE with a light chopper (0.2 s^{-1}). The measured photocurrent was derived as the difference between the dark and illuminated current values.

RESULTS AND DISCUSSION

Crystal Structure and Elemental Composition. To identify the crystal structure of the $SrNbO_2N$ film and the underlying TaN interfacial layer, X-ray diffraction was employed. For this purpose, thicker TaN (∼100 nm) and

https://doi.org/10.1021/acs.jpcc.1c10148
J. Phys. Chem. C 2022, 126, 5970−5979

$SrNbO_2N$ (~200 nm) films were prepared on Si(100) substrates to obtain clear diffraction patterns. XRD patterns of fabricated TaN/Si, $SrNbO_2N$/TaN/Si, and nominally $SrNbO_2N$/Si (without TaN) were compared to the reference patterns of cubic-TaN (PDF 01-089-5196) and $SrNbO_2N$ (PDF 01-073-3224) (Figure 1a). The XRD pattern of TaN/Si

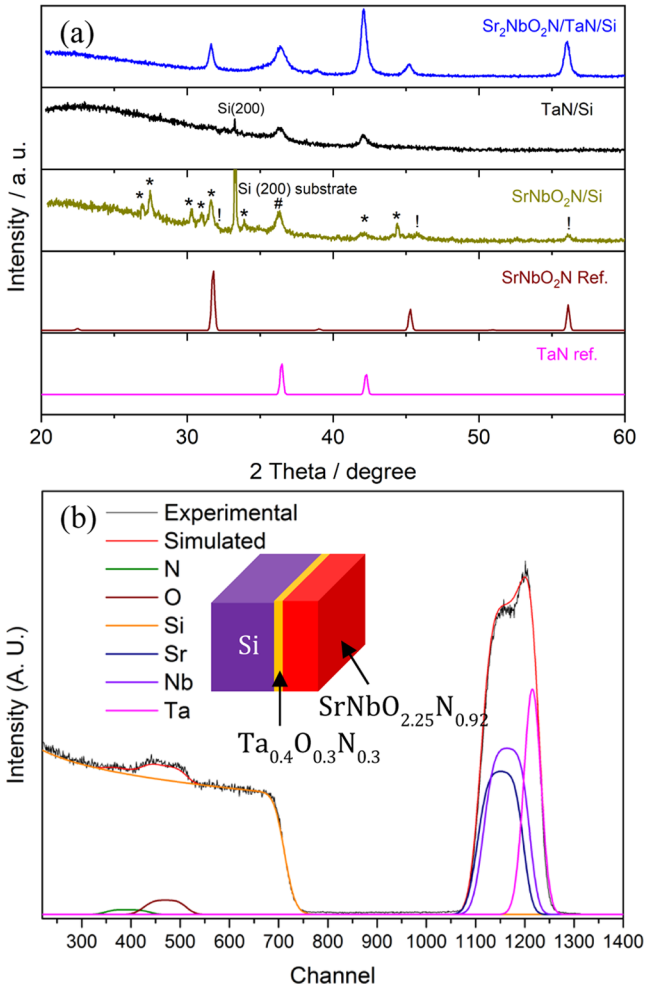

Figure 1. (a) X-ray diffraction for (top to bottom) $SrNbO_2N$/TaN/Si, TaN/Si, and $SrNbO_2N$/Si (without TaN) and reference patterns of $SrNbO_2N$ and cubic-TaN. Star symbol (*) matches with Sr_2SiO_4 reference patterns (PDF 01-076-1493), and exclamation symbol (!) matches with $SrNbO_2N$ reference patterns (PDF 01-073-3224). The hash symbol (#) indicates an unknown peak. (b) Rutherford backscattering spectrum of the $SrNbO_2N$/TaN/Si film. A simulated model was used to match the experimental $SrNbO_2N$/TaN/Si data.

(black) is matched with the reference pattern of cubic-TaN (magenta), indicating that the given deposition conditions are capable of forming pure-phase cubic-TaN. When high-temperature ammonolysis of a $SrNbO_x$ film on Si is performed without a TaN diffusion barrier, the diffraction pattern (Figure 1a yellow-green) shows Sr_2SiO_4 as a dominant phase with a minor contribution from $SrNbO_2N$, as well as a Si(200) substrate peak and one unknown peak. Alternately, $SrNbO_2N$/TaN films (blue) have high crystallinity, and the diffraction patterns of $SrNbO_2N$ are well-matched with $SrNbO_2N$ reference patterns without undesired impurities such as $TaSi_2$ or Sr_2SiO_4, confirming that the fabricated film is phase pure. This demonstrates that TaN is necessary for forming pure-phase $SrNbO_2N$. In a later section, we will discuss the effectiveness of ultrathin TaN films as a diffusion barrier.

The elemental composition of the $SrNbO_2N$ film was measured by Rutherford backscattering spectroscopy (RBS) on a thick $SrNbO_2N$ film (~200 nm) with the ultrathin TaN film (5.5 nm). These thicknesses are used for later characterization and photoelectrochemical evaluation, except when deliberately varying the $SrNbO_2N$ thickness. It is also worth noting that the ultrathin TaN film helps to minimize the interference of the Ta signal with those of Sr and Nb, which can overlap with thicker Ta-based films in RBS spectra. Figure 1b indicates that the composition of the sample can be described as a single layer of the approximate composition of $SrNbO_{2.25}N_{0.92}$ with a thin interfacial layer of $Ta_{0.4}N_{0.3}O_{0.3}$ and a Si substrate. The equal ratio of Sr to Nb confirms the PLD target deposition and that the postannealing treatment does not cause significant conversion of the perovskite to form SrO_x or NO_xN. RBS indicates that the Si substrate does not diffuse out to the surface during ammonolysis. RBS results also demonstrate the introduction of N in the film; however, the strong background from the Si substrate decreases the accuracy of N determination.[28] More detailed analysis of anion species is described below.

Chemical States of $SrNbO_2N$ and TaN Films. Probing the chemical states of $SrNbO_2N$ is important to identify defects (e.g., Nb^{4+}) that can act as trap sites during photoelectrochemical reactions.[14,26] Figure 2a–d shows the XPS core-level spectra of Nb 3d, Sr 3d, N 1s, and O 1s. In the $SrNbO_2N$ film, the Sr 3d spectra were deconvoluted to a sharp doublet at binding energies 135.3 and 133.6 eV, attributable to the spin–orbit split Sr $3d_{3/2}$ and Sr $3d_{5/2}$ states, respectively, for Sr^{2+}.[29] The Nb 3d spectra consist of a sharp doublet at 206.5 and 209.2 eV corresponding to the expected spin–orbit coupled $3d_{5/2}$ and $3d_{3/2}$ states, respectively. The shape, intensity, and location of this doublet are similar to that reported for Nb^{5+} in bulk $Sr_2Nb_2O_7$[30] and $SrNbO_2N$.[31] Further confirmation of the Nb^{5+} valence comes from a report showing that this doublet matches that reported in a recent study of Mg-doped $SrNbO_2N$, which claimed substantial suppression of Nb^{4+} after substitution of Mg in the B site.[15] For the N 1s core-level spectra, the observed peak with binding energy near 396 eV demonstrates the substitution of lattice nitride (N^{3-}) into the oxide lattice, which is quite distinct from that caused by more weakly adsorbed surface nitrogen.[10] The strong N 1s peak and the absence of Nb^{4+} indicate that the fabricated films have the stoichiometry $SrNbO_{3-x}N_x$ (x = 0.96–1.02).[32] This composition is also supported by the O 1s spectra showing two features: a dominant lattice O^{2-} and a smaller surface absorbed OH^- centered at binding energies of 530.1 and 531.8 eV, respectively. XPS analysis of the TaN/Si sample was performed and confirms that the major Ta oxidation state is close to that expected for Ta^{3+} (23.8 eV), and it contains lattice nitrogen as nitride N^{3-} (396.9 eV) (Figure 2e,f).

Optical Properties of $SrNbO_2N$ and TaN Films. UV–vis diffuse reflectance was employed to determine the band gap of the $SrNbO_2N$ thin film using the Tauc plot (Figure 3a). The spectra show that $SrNbO_2N$ has an indirect optical band gap of 1.9 eV, which is similar to those previously reported.[15,33] In addition, the spectra have a relatively short tail at a wavelength higher than 700 nm. The weak long-wavelength absorption tail has been explained as either niobium reduction during ammonolysis or defects.[6] IR light scattering due to the grain

https://doi.org/10.1021/acs.jpcc.1c10148
J. Phys. Chem. C 2022, 126, 5970–5979

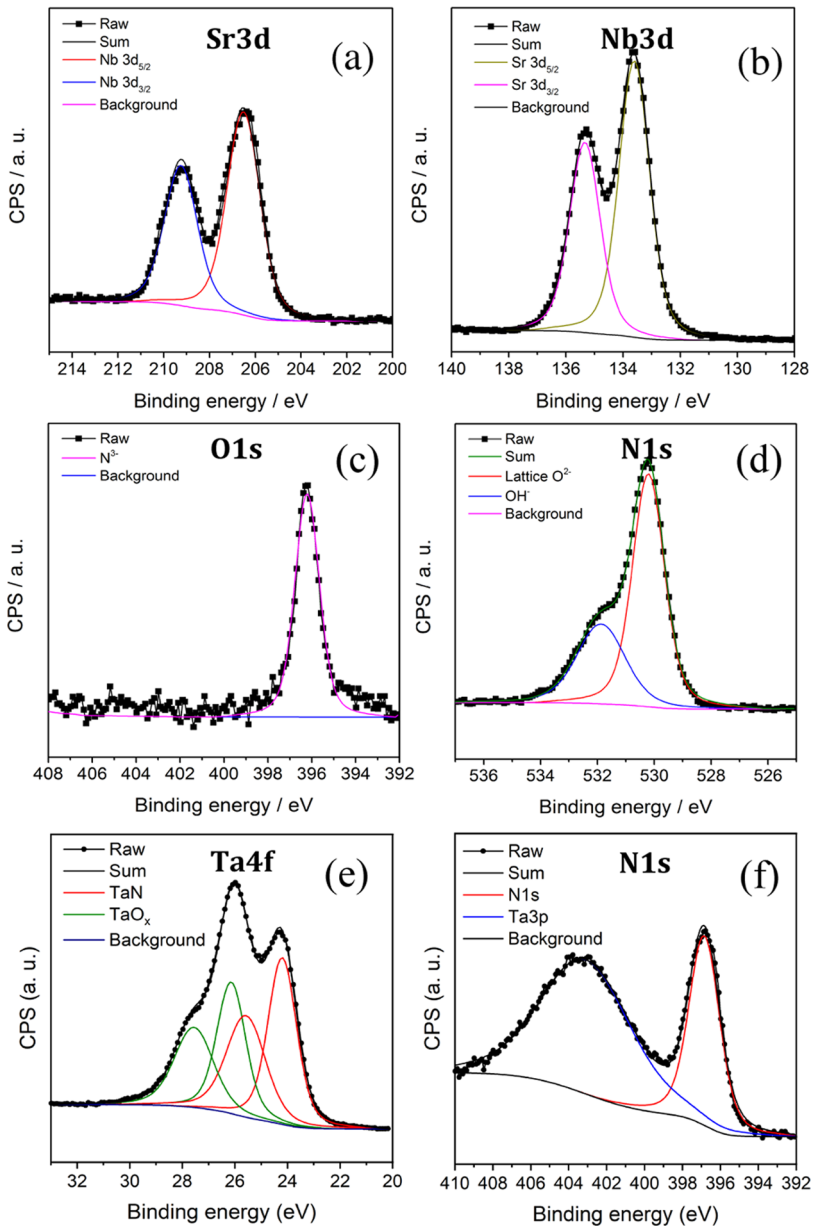

Figure 2. X-ray photoelectron core-level spectra of (a) Sr 3d, (b) Nb 3d, (c) O 1s, and (d) N 1s for the $SrNbO_2N$/TaN/Si film and (e) Ta 4f and (f) N 1s for the TaN/Si film.

size refraction also contributes. In addition to the Tauc method, we additionally confirmed the optical edge by IPCE measurement, which clearly shows an IPCE close to 0% above 650 nm wavelength. Low absorption (high transmission) at long wavelengths (near IR) is a necessary property for the larger band gap material in tandem photoabsorber devices, and the optical measurement, as shown in Figures 3a and S1, demonstrates that fabricated $SrNbO_2N$ films are suitable for this purpose.

The optical properties of ultrathin films of TaN were also evaluated using reflectance and transmittance measurements. Since c-TaN has metallic properties,[34] it is expected to absorb the light across the UV−vis−IR range. Full optical measurements of the 5.5 nm TaN/quartz sample show that TaN absorbs light in the range of 30−35% of incident light (Figure 3b). This is not a negligible contribution, but managing overall optical properties (e.g., decreased total reflectance) for $SrNbO_2N$/ultrathin TaN films on the bottom photoabsorber (e.g., Si) is expected to compensate for the overall loss and achieve optimum tandem PEC performance.

Film Morphologies and Roughness Factor. The surface structure is often crucial in photoelectrochemical performance and can dictate the device design. A helium ion microscope (HIM) was used to probe film morphologies and film thickness by top (plan view) and cross-sectional views, respectively. Figure S1a,b shows a top view of HIM images for the Si substrate and TaN/Si. The featureless image of the ultrathin TaN film indicates that it is pin-hole free and follows the atomically smooth morphology of the Si(100) substrate. Cross-sectional HIM images of a 100 nm $SrNbO_2N$/TaN/Si structure, as shown in Figure 4a, demonstrate that the thickness of TaN is approximately 5.5 nm, and it uniformly coats the Si substrate. Compared to our previous study using the TiN diffusion barrier,[19] both $SrNbO_2N$/TaN and TaN/Si

https://doi.org/10.1021/acs.jpcc.1c10148
J. Phys. Chem. C 2022, 126, 5970−5979

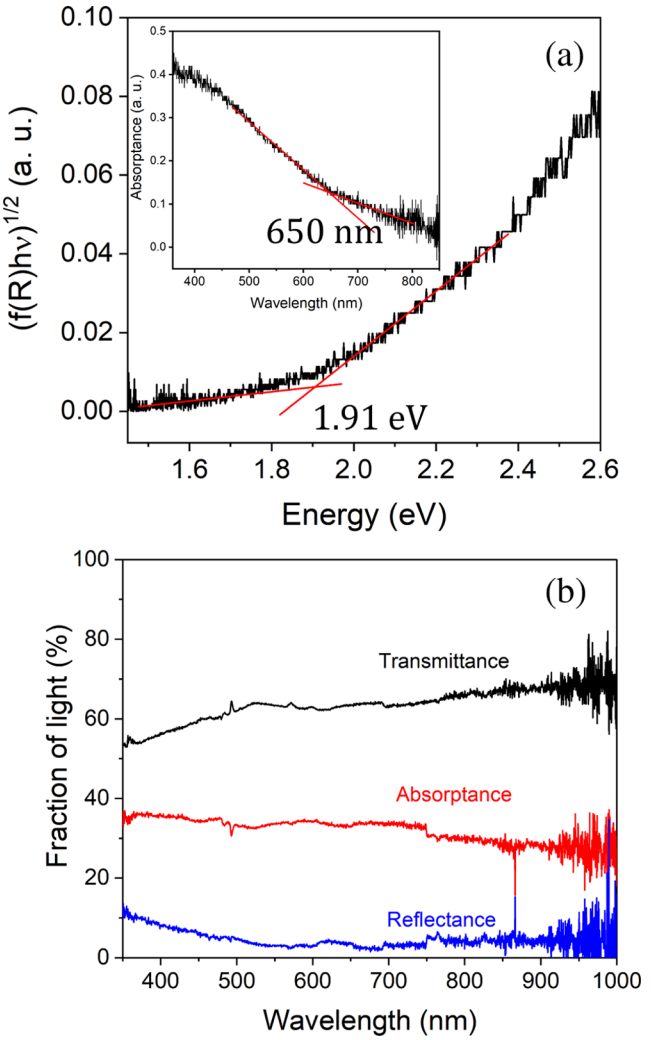

Figure 3. (a) Tauc plot and UV−vis diffuse reflectance (inset) of the $SrNbO_2N$ thin film. The inflection in the absorptance and Tauc plots was determined by the intersection of the two lines determined by linear regression. (b) Optical properties of 5.5 nm TaN on the quartz substrate.

interfaces appear sharp, which clearly show that this thickness is sufficient to prevent atomic interdiffusion during high-temperature ammonolysis.

Figure 4b−f shows the morphologies of the $SrNbO_2N$ thin films in the range of 20−400 nm thickness. When the thickness of the $SrNbO_2N$ film is less than 100 nm (Figure 4b,c), the surface is made up of 10−20 nm diameter nearly spherical grains. For thicker films, >150 nm, the images (Figure 4d−f) show nonspherical grains, with dimensions varying between 10 and 100 nm for any given grain. A similar feature can be found in the cross-sectional images (Figure S2), where film thickness > 150 nm starts to add porosity to the structure due to larger grain sizes. Both top and cross-sectional views indicate that increasing the deposition time of the PLD process not only changes the thickness but also modifies the grain size, morphology, and packing (porosity).

In addition to HIM, non-Faradaic electrochemical capacitance measurements were performed on $SrNbO_2N$ films to investigate film roughness.[35] Capacitive currents were measured between 0.7 and 0.9 V vs RHE, where no Faradaic process occurs under dark conditions. Plots of capacitive current density vs scan rate, shown in Figure 5, give the

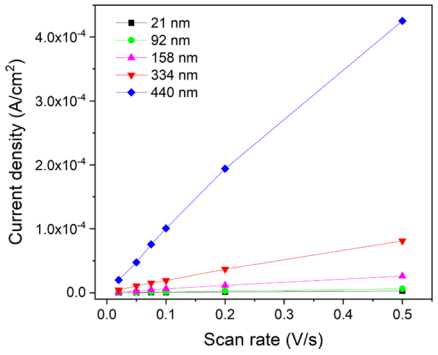

Figure 5. Electrochemical capacitive current density vs scan rate for different thicknesses of $SrNbO_2N$ thin films.

capacitance/area and roughness factor. These are tabulated vs thickness in Table 1. Similar to grain size observations, as the

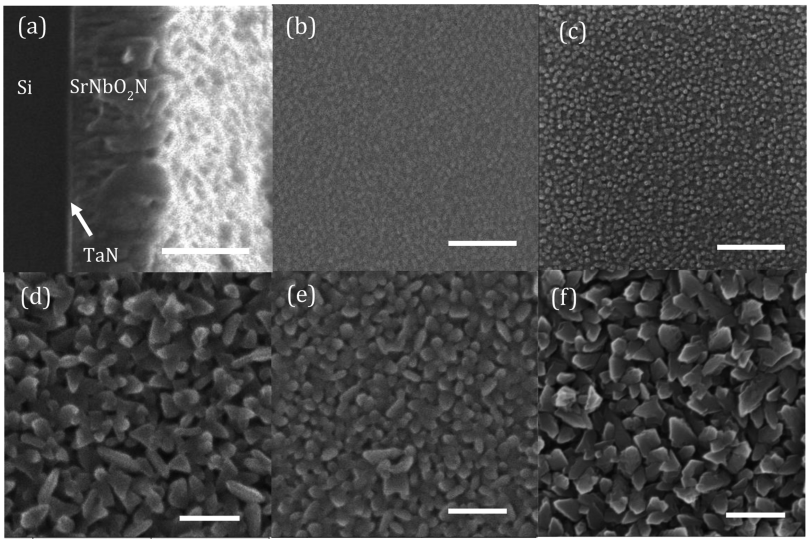

Figure 4. Helium ion microscope (HIM) images: (a) cross-sectional view of 158 nm $SrNbO_2N$/TaN/Si, (b) 21 nm $SrNbO_2N$/TaN/Si, (c) 92 nm $SrNbO_2N$/TaN/Si, (d) 158 nm $SrNbO_2N$/TaN/Si, (e) 334 nm $SrNbO_2N$/TaN/Si, and (f) 440 nm $SrNbO_2N$/TaN/Si. All scale bars are 200 nm.

https://doi.org/10.1021/acs.jpcc.1c10148
J. Phys. Chem. C 2022, 126, 5970−5979

Table 1. Roughness Factor of Each $SrNbO_2N$ Thickness Measured by Electrochemical Capacitance

samples	(a)	(b)	(c)	(d)	(e)
thickness (nm)	21 ± 2	92 ± 3	158 ± 5	334 ± 8	440 ± 9
roughness factor	0.14	0.31	1.30	4.00	21.00

thickness of the film increases, the roughness factor increases nonlinearly. It ranges from very small (<1) below 100 nm and increases at 150 nm. At a thickness of 440 nm, the roughness factor is 20, where images reveal the formation of large grains with increased porosity (Figures 4d–f and S2).

Energy-Level Diagram of the $SrNbO_2N$ Film. Understanding the valence and conduction electronic states of thin-film semiconductors provides key diagnostic information for evaluating photoelectrochemical water splitting activity and electrode stability/corrosion. In addition to the UV–vis spectra in Figure 3a, we used valence-resolved XPS and electrochemical impedance spectroscopy (Mott–Schottky plot, MS) to determine the band alignments.[7,15] Two implicit assumptions were made in our measurements: significant chemical changes do not occur on going from the surface to bulk, and grain boundary charging in these samples is negligible. In the valence XPS spectra, the threshold for the valence band absorption was observed at −1.76 eV vs zero binding energy (Figure S3a). This observed E_F to E_{VB} energy spacing is consistent with other compounds in this class, where $ATa(O,N)_3$ (A = Ca, Sr, Ba, Pr^{3+}) ranges from 0.85 to 2.84 eV.[36]

Figure S3b shows a Mott–Schottky (MS) plot of a $SrNbO_2N$ thin film in a 0.1 M KOH (pH 13) electrolyte. An MS plot enables the determination of the limiting potential extrapolated to infinite capacitance. The E_{Fb} extracted from the MS plot is 0.02 V vs RHE, which corresponds to E_F = −4.42 eV vs E_{Vac}. From this analysis emerges a complete picture of the valence and conduction levels of $SrNbO_2N$, as shown in Figure 6. The Fermi level position lies near the top of the band

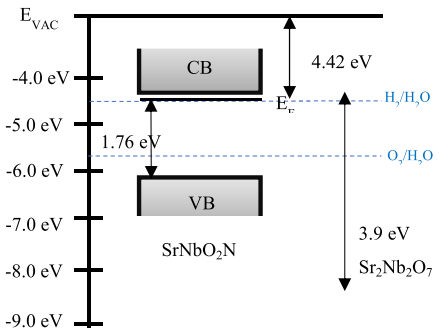

Figure 6. Composite, experimental energy states for $SrNbO_2N$ compared to E_{vac} and the water redox potentials. The E_g is from UV–vis DRS, VB to E_F is from XPS, and EF is the MS plot, which allow the estimation of energy levels of $SrNbO_2N$. The band gap (3.9 eV) and estimated band edges of $Sr_2Nb_2O_7$ were reported in ref 30.

gap, indicating that this semiconductor is n-type. The absolute conduction and valence band edge positions can be compared to the vacuum level (E_{vac}) and to the potential for water oxidation (−5.67 eV).[37] The conduction band minimum (CBM) is located at −4.42 eV vs E_{vac}. The valence band maximum (VBM) is located more negative (>0.5 eV) than the water oxidation potential. With its near-optimal band gap and valence band maximum (VBM) position lower than the water oxidation potential, this material can be used as a photoanode to drive water oxidation in a tandem device.

Comparing $SrNbO_2N$ to $Sr_2Nb_2O_7$,[38] the addition of nitrogen 2p orbitals significantly decreases the band gap from 3.9 to 1.9 eV and shifts the VBM more than 1 eV[36] (also summarized in Figure 6).

Photoelectrochemical Performance. To determine the influence of $SrNbO_2N$ film thickness and roughness on intrinsic photoelectrochemical performance, potassium ferrocyanide ($K_4[Fe(CN)_6]$) was used without a catalyst layer. This is a necessary simplification to obtain the performance metrics solely for the photoabsorber. Considering the standard potential for $[Fe(CN)_6]^{4-}$ and O_2[37] as well as the absence of oxygen evolution reaction catalysts, we expect that all of the photocurrent comes from $[Fe(CN)_6]^{4-}$ oxidation. This reversible one-electron redox process avoids kinetic losses during the four-electron water oxidation process.[39] AM 1.5G simulated sunlight was used in all reported photoelectrochemical measurements. Since this redox couple absorbs blue light, it is expected to change the incident light intensity. To measure the actual loss caused by absorption, we recorded spectral irradiance with and without the redox couple. Figure S4 shows that a given concentration of ferro/ferricyanide results in a 20% power loss between 350 and 465 nm under measurement conditions.

To assess the influence of different thicknesses and roughness on intrinsic photoelectrochemical performance, we performed linear sweep voltammetry (LSV) and determined the open-circuit potential (OCP) under illumination and dark conditions. LSV can determine the onset potential and photocurrent density, while OCP measures photovoltage (V_{ph}). Figure 7a shows the LSVs of illuminated and dark $SrNbO_2N$ films of thicknesses 21, 92, 158, 334, and 440 nm. The onset potential of 21 and 92 nm thick films was around 0.9 V vs RHE, whereas for films of 158, 334, and 440 nm thickness, the onset potential was near 0.73 V vs RHE at 0.05 mA/cm^2. As expected for the semiconductor, no significant dark current was observed within the potential window used for testing. To evaluate photovoltage (V_{ph}), the difference between the OCP with and without illumination was measured (Figure 7b,c). Similar to the results for the onset potential, the 21 and 92 nm thick films have similar photovoltages (averaged 190 mV). The highest averaged V_{ph} of 337 mV was obtained for the 334 nm thick film, which is similar to that of the 440 nm thick film at 325 mV. Based on these results, $SrNbO_2N$ thin films can generate photovoltages comparable to other unmodified metal-oxide and metal-nitride semiconductors (250–700 mV).[40−42]

The photocurrent density is another important factor that is directly proportional to solar-to-hydrogen efficiency.[39,43] We defined the photocurrent density as a difference of measured value at an applied bias of 1.23 V vs RHE under illumination and dark conditions to eliminate the current density that arises from surface charge under bias. The photocurrent density as a function of thickness is plotted in Figure 7c. The graph shows a sharp maximum at 334 nm thickness (0.73 mA/cm^2), identical to the thickness dependence of photovoltage, but decreases more sharply as the thickness increases further. The former result is attributable to increasing current due to greater light absorption by $SrNbO_2N$, which has an absorption length of ∼1 μm in this spectral range.[20] At larger thicknesses, both roughness and grain size[18] increase as quantified by HIM

https://doi.org/10.1021/acs.jpcc.1c10148
J. Phys. Chem. C 2022, 126, 5970−5979

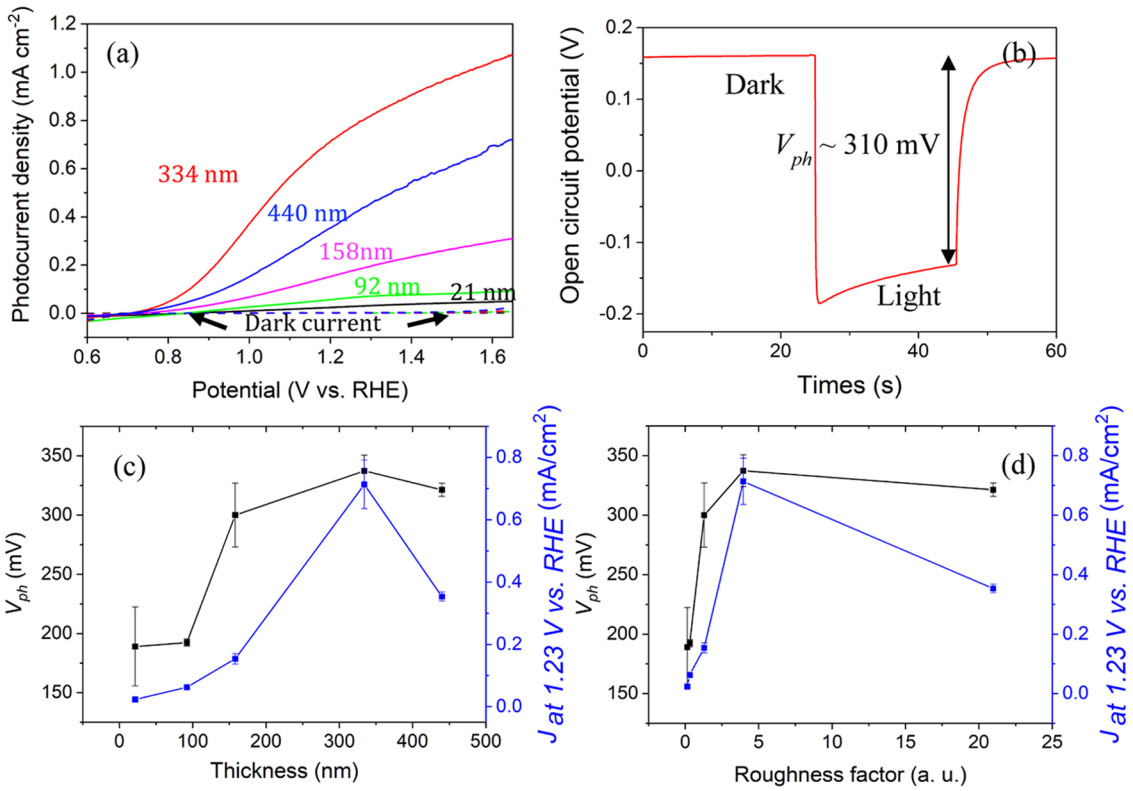

Figure 7. (a) Photoelectrochemical ferrocyanide oxidation of $SrNbO_2N$ films of different thicknesses on TaN/Si. The scan rate is 10 mV/s. (b) Example of photovoltage measurement using the open-circuit potential (OCP) under light and dark conditions. Photovoltage and photocurrent density at 1.23 V vs RHE as a function of (c) thickness and (d) roughness factor.

images, resulting in greater current losses from particle sizes greater than the charge carrier diffusion length.

In addition, other factors also need to be considered. For example, the surface roughness is directly related to the electrochemical surface area, which is linearly proportional to the current density.[44] By contrast, high surface areas can exacerbate surface recombination on photoabsorbers lacking efficient charge collection (interface with either a metallic layer or catalyst)[45,46] To evaluate the contribution from grain size and porosity of $SrNbO_2N$ films, the photocurrent density and photovoltage are plotted as a function of roughness factor (Figure 7d). Both photovoltage and photocurrent density increase linearly up to a roughness factor of ~5 and then decrease between 5 and 20.

Based on these and the earlier thickness dependence results, we can explain the PEC performance of $SrNbO_2N$ trends as follows: from the results of morphology (HIM images) as well as photovoltage and photocurrent dependence on the thickness and roughness factor, we can conclude that the surface area and absorption length are the dominant factors determining PEC performance at thicknesses up to approximately 150 nm. This arises from insufficient light absorption, although the grain size is not a limiting factor as it is smaller than the minority carrier diffusion length. By contrast, for thicknesses above 300 nm, the larger grain size exceeds the carrier diffusion length and recombination (out)competes. Based on these results, a 150−300 nm $SrNbO_2N$ film is recommended to achieve good light absorption without compromising carrier diffusion to the surface. Although the surface area (as measured by roughness, porosity, and grain size) and photoabsorber thickness could not be independently controlled, using this approach, both variables contribute appreciably to PEC performance.

Nanostructured Substrates (Controlling Roughness Alone). Nanostructuring is an effective means to increase the photocurrent density of photoabsorbers that suffer from a short carrier diffusion length.[40,47] In a tandem PEC device, it is possible to use this approach to control the photocurrents in the two half cells that need to be matched to achieve the highest STH efficiency.[48,49] To isolate the surface area contribution, we prepared $SrNbO_2N$ thin films on a pyramidal nanostructured Si substrate. The pyramidal structure allows one to increase the surface area 2−3 times while maintaining the thickness and morphology of the $SrNbO_2N$ film similar to that on flat Si. Figure 8a−d shows HIM images of the top and cross-sectional view of $SrNbO_2N$ films on a pyramidal structured film and compared it with a flat Si substrate. The width and height of the pyramid are in the range of 0.1−3 and 2−3 μm, respectively. This footprint indeed creates a 2−3-fold increase in the surface area and corroborates well with electrochemically active surface area measurements (Figure S4 and Table S1). The thickness of the $SrNbO_2N$ on both substrates was fabricated close to 100 nm to rule out differences in the carrier diffusion length, but slightly increased absorption by the structured Si substrate cannot be fully ruled out. Figure 8e compares the LSVs of $SrNbO_2N$ thin films (approx. 100 nm) prepared on planar vs pyramidal structured Si. The measured photocurrent densities (at 1.23 V vs RHE) of planar and structured substrates under illumination are 0.06 and 0.2 mA/cm^2, respectively. The results indicate that the photocurrent density is linearly proportional to the surface area at a given thickness. This demonstrates that the surface area

https://doi.org/10.1021/acs.jpcc.1c10148
J. Phys. Chem. C 2022, 126, 5970−5979

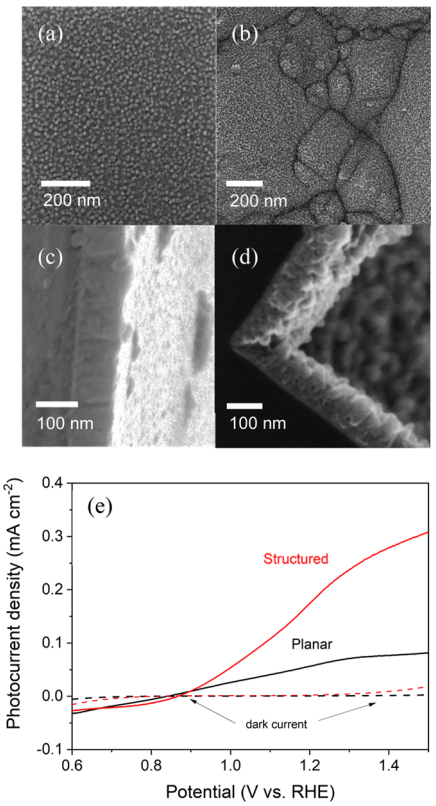

Figure 8. HIM images of the top and cross-sectional views of a $SrNbO_2N$ thin film fabricated on planar (a, c) and structured (b, d) Si substrates. (e) Photoelectrochemical ferrocyanide oxidation of a $SrNbO_2N$ thin film fabricated on structured and planar Si substrates. The scan rate is 10 mV/s.

can be an important parameter to tune the photocurrent density of $SrNbO_2N$.

CONCLUSIONS

In this work, we synthesized polycrystalline $SrNbO_2N$ thin films on Si substrates and demonstrated that they can potentially function in a tandem photoabsorber configuration with Si, if the film thickness, surface area, elemental stoichiometry, and morphology are properly controlled. An ultrathin film of TaN was used as an effective diffusion barrier that allows high-temperature ammonolysis to convert an oxide into an oxynitride thin film without atomic interdiffusion into Si. The PEC performance as a function of thickness and roughness reveals that the absorption length and surface area govern the PEC performance at a thickness (or grain size) below 150 nm, whereas limited carrier diffusion length competes and lowers PEC performance at and above 300 nm. We have demonstrated that controlling the surface morphology of the photoabsorber is an effective strategy to tune the photocurrent density of different layers in a tandem configuration.

We believe that the strategy used to develop low-cost, tandem PEC devices based on combining high-temperature oxynitrides on silicon realized by developing TaN as a diffusion barrier can be extended to a similar class of materials in the PEC device community.

ASSOCIATED CONTENT

Supporting Information

The Supporting Information is available free of charge at https://pubs.acs.org/doi/10.1021/acs.jpcc.1c10148.

IPCE data; cross-sectional HIM images; XPS valence band spectra and MS plot of a $SrNbO_2N$ film; spectra irradiance of light and comparison with a ferricyanide electrolyte; and electrochemical capacitive current density of planar and structured $SrNbO_2N$ with their calculated roughness factor (PDF)

AUTHOR INFORMATION

Corresponding Authors

Martha Greenblatt − *Department of Chemistry & Chemical Biology, Rutgers, Piscataway, New Jersey 08854, United States;* orcid.org/0000-0002-1806-2766; Email: greenbla@chem.rutgers.edu

Eric Garfunkel − *Department of Chemistry & Chemical Biology, Rutgers, Piscataway, New Jersey 08854, United States; Department of Physics & Astronomy, Rutgers, The State University of New Jersey, Piscataway, New Jersey 08854, United States*; Email: egarf@chem.rutgers.edu

G. Charles Dismukes − *Department of Chemistry & Chemical Biology, Rutgers, Piscataway, New Jersey 08854, United States; Waksman Institute, Rutgers University, Piscataway, New Jersey 08854, United States;* orcid.org/0000-0003-0155-0541; Email: dismukes@chem.rutgers.edu

Authors

Shinjae Hwang − *Department of Chemistry & Chemical Biology, Rutgers, Piscataway, New Jersey 08854, United States;* orcid.org/0000-0001-5442-8609

Spencer H. Porter − *Department of Chemistry & Chemical Biology, Rutgers, Piscataway, New Jersey 08854, United States*

Mengjun Li − *Department of Chemistry & Chemical Biology, Rutgers, Piscataway, New Jersey 08854, United States*

Ryan Thorpe − *Department of Physics & Astronomy, Rutgers, The State University of New Jersey, Piscataway, New Jersey 08854, United States*

Anders B. Laursen − *Department of Chemistry & Chemical Biology, Rutgers, Piscataway, New Jersey 08854, United States; Waksman Institute, Rutgers University, Piscataway, New Jersey 08854, United States;* orcid.org/0000-0002-1386-9202

Hengfei Gu − *Department of Chemistry & Chemical Biology, Rutgers, Piscataway, New Jersey 08854, United States*

Ahmad Safari − *Department of Materials Science & Engineering, Rutgers University, Piscataway, New Jersey 08854, United States*

Complete contact information is available at: https://pubs.acs.org/10.1021/acs.jpcc.1c10148

Notes

The authors declare no competing financial interest.

ACKNOWLEDGMENTS

This work was supported by a joint DOE-EERE (Energy Efficiency and Renewable Energy)/NSF-CBET (Chemical, Bioengineering, Environmental, and Transport systems) award number 1433492 and a continuation award from DOE-EERE

number DE-EE0008083. The authors thank Dr. Peter Khalifah for the helpful discussion during the early stages of this project.

REFERENCES

(1) Lewis, N. S.; Nocera, D. G. Powering the Planet: Chemical Challenges in Solar Energy Utilization. *Proc. Natl. Acad. Sci. U.S.A.* **2006**, *103*, 15729−15735.
(2) Yu, Q.; Meng, X.; Wang, T.; Li, P.; Liu, L.; Chang, K.; Liu, G.; Ye, J. A Highly Durable P-LaFeO3 /N-Fe2O3 Photocell for Effective Water Splitting Under Visible Light. *Chem. Commun.* **2015**, *51*, 3630−3633.
(3) Berglund, S. P.; Abdi, F. F.; Bogdanoff, P.; Chemseddine, A.; Friedrich, D.; van de Krol, R. Comprehensive Evaluation of CuBi2O4 as a Photocathode Material for Photoelectrochemical Water Splitting. *Chem. Mater.* **2016**, *28*, 4231−4242.
(4) Chen, Y.-S.; Manser, J. S.; Kamat, P. V. All Solution-Processed Lead Halide Perovskite-BiVO4 Tandem Assembly for Photolytic Solar Fuels Production. *J. Am. Chem. Soc.* **2015**, *137*, 974−981.
(5) Kuang, Y.; Jia, Q.; Nishiyama, H.; Yamada, T.; Kudo, A.; Domen, K. A Front-Illuminated Nanostructured Transparent BiVO4 Photoanode for >2% Efficient Water Splitting. *Adv. Energy Mater.* **2016**, *6*, No. 1501645.
(6) Porter, S. H.; Huang, Z.; Woodward, P. M. Study of Anion Order/Disorder in RTaN2O (R = La, Ce, Pr) Perovskite Nitride Oxides. *Chem. Mater.* **2014**, *14*, 117−125.
(7) Porter, S. H.; Huang, Z.; Dou, S.; Brown-Xu, S.; Sarwar, A. T. M. G.; Myers, R. C.; Woodward, P. M. Electronic Structure and Photocatalytic Water Oxidation Activity of RTiNO2 (R = Ce, Pr, and Nd) Perovskite Nitride Oxides. *Chem. Mater.* **2015**, *27*, 2414−2420.
(8) Seo, J.; Nishiyama, H.; Yamada, T.; Domen, K. Visible-Light-Responsive Photoanodes for Highly Active, Stable Water Oxidation. *Angew. Chem., Int. Ed.* **2018**, *57*, 8396−8415.
(9) Higashi, M.; Domen, K.; Abe, R. Fabrication of an Efficient BaTaO2N Photoanode Harvesting a Wide Range of Visible Light for Water Splitting. *Cryst. Growth Des.* **2013**, *135*, 10238−10241.
(10) Maeda, K.; Higashi, M.; Siritanaratkul, B.; Abe, R.; Domen, K. SrNbO 2N as a Water-Splitting Photoanode with a Wide Visible-Light Absorption Band. *J. Am. Chem. Soc.* **2011**, *133*, 12334−12337.
(11) Kasahara, A.; Nukumizu, K.; Hitoki, G.; Takata, T.; Kondo, J. N.; Hara, M.; Hisayoshi Kobayashi, A.; Domen, K. Photoreactions on LaTiO2N Under Visible Light Irradiation. *J. Phys. Chem. A* **2002**, *106*, 6750−6753.
(12) Castelli, I. E.; Olsen, T.; Datta, S.; Landis, D. D.; Dahl, S.; Thygesen, K. S.; Jacobsen, K. W. Computational Screening of Perovskite Metal Oxides for Optimal Solar Light Capture. *Energy Environ. Sci.* **2012**, *5*, 5814−5819.
(13) Kim, Y.; Woodward, P. M.; Baba-Kishi, K. Z.; Tai, C. W. Characterization of the Structural, Optical, and Dielectric Properties of Oxynitride Perovskites AMO2N (a = Ba, Sr, Ca; M = Ta, Nb). *Chem. Mater.* **2004**, *16*, 1267−1276.
(14) Kawashima, K.; Hojamberdiev, M.; Mabayoje, O.; Wygant, B. R.; Yubuta, K.; Mullins, C. B.; Domen, K.; Teshima, K. NH3-Assisted Chloride Flux-Coating Method for Direct Fabrication of Visible-Light-Responsive SrNbO2 N Crystal Layers. *CrystEngComm* **2017**, *19*, 5532−5541.
(15) Sun, X.; Liu, G.; Xu, X. Defect Management and Efficient Photocatalytic Water Oxidation Reaction Over Mg Modified SrNbO2N. *J. Mater. Chem. A* **2018**, *6*, 10947−10957.
(16) Kodera, M.; Urabe, H.; Katayama, M.; Hisatomi, T.; Minegishi, T.; Domen, K. Effects of Flux Synthesis on SrNbO2N Particles for Photoelectrochemical Water Splitting. *J. Mater. Chem. A* **2016**, *4*, 7658−7664.
(17) Hiralal, P.; Saremi-Yarahmadi, S.; Bayer, B. C.; Wang, H.; Hofmann, S.; Upul Wijayantha, K. G.; Amaratunga, G. A. J. Nanostructured Hematite Photoelectrochemical Electrodes Prepared by the Low Temperature Thermal Oxidation of Iron. *Sol. Energy Mater. Sol. Cells* **2011**, *95*, 1819−1825.
(18) Pinaud, B. A.; Vesborg, P. C. K.; Jaramillo, T. F. Effect of Film Morphology and Thickness on Charge Transport in Ta3N5/Ta Photoanodes for Solar Water Splitting. *J. Phys. Chem. Lett.* **2012**, *116*, 15918−15924.
(19) Porter, S. H.; Hwang, S.; Amarasinghe, V.; Taghaddos, E.; Manichev, V.; Li, M.; Gardner, G.; Safari, A.; Garfunkel, E.; Greenblatt, M.; Dismukes, G. C. Optimizing "Artificial Leaf" Photoanode-Photocathode-Catalyst Interface Systems for Solar Water Splitting. *ECS Trans.* **2016**, *72*, 1−19.
(20) Kikuchi, R.; Nakamura, T.; Tamura, S.; Kaneko, Y.; Hato, K. Fundamental Semiconducting Properties of Perovskite Oxynitride SrNbO2N: Epitaxial Growth and Characterization. *Cryst. Growth Des.* **2017**, *29*, 7697−7703.
(21) Rossnagel, S. M.; Kim, H. Diffusion Barrier Properties of Very Thin TaN with High Nitrogen Concentration. *J. Vac. Sci. Technol., B* **2003**, *21*, 2550−2554.
(22) Kwon, J.-D.; Jeong, S.-J.; Kang, J.-W.; Kim, D.-G.; Kim, J.-K.; Rha, J.-J.; Nam, K.-S.; Kwon, S.-H. Low Temperature Two-Step Atomic Layer Deposition of Tantalum Nitride for Cu Diffusion Barrier. *J. Electrochem. Soc.* **2009**, *156*, H832−H835.
(23) Hwang, S.; Porter, S. H.; Laursen, A. B.; Yang, H.; Li, M.; Manichev, V.; Calvinho, K. U. D.; Amarasinghe, V.; Greenblatt, M.; Garfunkel, E.; Dismukes, G. C. Creating Stable Interfaces Between Reactive Materials: Titanium Nitride Protects Photoabsorber−Catalyst Interface in Water-Splitting Photocathodes. *J. Mater. Chem. A* **2019**, *7*, 2400−2411.
(24) Hwang, S.; Young, J. L.; Mow, R.; Laursen, A. B.; Li, M.; Yang, H.; Batson, P. E.; Greenblatt, M.; Steiner, M. A.; Friedman, D.; et al. Highly Efficient and Durable III−v Semiconductor-Catalyst Photocathodes via a Transparent Protection Layer. *Sustainable Energy Fuels* **2020**, *3*, 1437−1442.
(25) Kim, H.; Lavoie, C.; Copel, M.; Narayanan, V.; Park, D. G.; Rossnagel, S. M. The Physical Properties of Cubic Plasma-Enhanced Atomic Layer Deposition TaN Films. *J. Appl. Phys.* **2004**, *95*, 5848−5855.
(26) Seo, J.; Moriya, Y.; Kodera, M.; Hisatomi, T.; Minegishi, T.; Katayama, M.; Domen, K. Photoelectrochemical Water Splitting on Particulate ANbO2N (a = Ba, Sr) Photoanodes Prepared From Perovskite-Type ANbO3. *Chem. Mater.* **2016**, *28*, 6869−6876.
(27) Mayer, M. *SIMNRA User's Guide*; Max-Planck-Institut für Plasmaphysik, 1997.
(28) Golecki, I. Rutherford Backscattering and Channeling Analysis of Epitaxial, Low-Mass Films on High-Mass Substrates. *Nucl. Instrum. Methods Phys. Res.* **1983**, *218*, 63−66.
(29) Ji, L.; McDaniel, M. D.; Wang, S.; Posadas, A. B.; Li, X.; Huang, H.; Lee, J. C.; Demkov, A. A.; Bard, A. J.; Ekerdt, J. G.; Yu, E. T. A Silicon-Based Photocathode for Water Reduction with an Epitaxial SrTiO3 Protection Layer and a Nanostructured Catalyst. *Nat. Nanotechnol.* **2015**, *10*, 84−90.
(30) Atuchin, V. V.; Grivel, J. C.; Korotkov, A. S.; Zhang, Z. Electronic Parameters of Sr2Nb2O7 and Chemical Bonding. *J. Solid State Chem.* **2008**, *181*, 1285−1291.
(31) Wang, J.; Wang, X.; Liu, B.; Li, X.; Cao, M. Facile Synthesis of SrNbO2N Nanoparticles with Excellent Visible-Light Photocatalytic Performances. *Mater. Lett.* **2015**, *152*, 131−134.
(32) Oka, D.; Hirose, Y.; Kaneko, M.; Nakao, S.; Fukumura, T.; Yamashita, K.; Hasegawa, T. Anion-Substitution-Induced Nonrigid Variation of Band Structure in $SrNbO_{3-x}N_x$ ($0 \le X \le 1$) Epitaxial Thin Films. *ACS Appl. Mater. Interfaces* **2018**, *10*, 35008−35015.
(33) Ebbinghaus, S. G.; Abicht, H.-P.; Dronskowski, R.; Müller, T.; Reller, A.; Weidenkaff, A. Perovskite-Related Oxynitrides—Recent Developments in Synthesis, Characterisation and Investigations of Physical Properties. *Prog. Solid State Chem.* **2009**, *37*, 173−205.
(34) Rossnagel, S. M. Characteristics of Ultrathin Ta and TaN Films. *J. Vac. Sci. Technol., B* **2002**, *20*, 2328−2336.
(35) Narkeviciute, I.; Jaramillo, T. F. Impact of Nanostructuring on the Photoelectrochemical Performance of Si/Ta3N5 Nanowire Photoanodes. *J. Phys. Chem. C* **2017**, *121*, 27295−27302.
(36) Balaz, S.; Porter, S. H.; Woodward, P. M.; Brillson, L. J. Electronic Structure of Tantalum Oxynitride Perovskite Photocatalysts. *Chem. Mater.* **2013**, *25*, 3337−3343.

https://doi.org/10.1021/acs.jpcc.1c10148
J. Phys. Chem. C 2022, 126, 5970−5979

(37) Trasatti, S. The Absolute Electrode Potential: an Explanatory Note (Recommendations 1986). *J. Electroanal. Chem.* **1986**, *58*, 955−966.
(38) Ebbinghaus, S. G.; Aguiar, R.; Weidenkaff, A.; Gsell, S.; Reller, A. Topotactical Growth of Thick Perovskite Oxynitride Layers by Nitridation of Single Crystalline Oxides. *Solid State Sci.* **2008**, *10*, 709−716.
(39) Narkeviciute, I.; Jaramillo, T. F. Effects of Ta3N5 Morphology and Composition on the Performance of Si-Ta3N5 Photoanodes. *Solar RRL* **2017**, *110*, No. 1700121.
(40) Narkeviciute, I.; Chakthranont, P.; Mackus, A. J. M.; Hahn, C.; Pinaud, B. A.; Bent, S. F.; Jaramillo, T. F. Tandem Core−Shell Si−Ta3N5 Photoanodes for Photoelectrochemical Water Splitting. *Nano Lett.* **2016**, *16*, 7565−7572.
(41) He, Y.; Thorne, J. E.; Wu, C. H.; Ma, P.; Du, C.; Dong, Q.; Guo, J.; Wang, D. What Limits the Performance of Ta3N5 for Solar Water Splitting? *Chem* **2016**, *1*, 640−655.
(42) Huang, W.; Harnagea, C.; Tong, X.; Benetti, D.; Sun, S.; Chaker, M.; Rosei, F.; Nechache, R. Epitaxial Bi2FeCrO6 Multiferroic Thin-Film Photoanodes with Ultrathin P-Type NiO Layers for Improved Solar Water Oxidation. *ACS Appl. Mater. Interfaces* **2019**, *11*, 13185−13193.
(43) Prévot, M. S.; Sivula, K. Photoelectrochemical Tandem Cells for Solar Water Splitting. *J. Phys. Chem. C* **2013**, *117*, 17879−17893.
(44) McCrory, C. C. L.; Jung, S.; Ferrer, I. M.; Chatman, S. M.; Peters, J. C.; Jaramillo, T. F. Benchmarking Hydrogen Evolving Reaction and Oxygen Evolving Reaction Electrocatalysts for Solar Water Splitting Devices. *J. Am. Chem. Soc.* **2015**, *137*, 4347−4357.
(45) Zhu, K.; Kopidakis, N. Influence of Surface Area on Charge Transport and Recombination in Dye-Sensitized TiO2 Solar Cells. *J. Phys. Chem. B* **2006**, *110*, 25174−25180.
(46) Oh, J.; Yuan, H.-C.; Branz, H. M. An 18.2%-Efficient Black-Silicon Solar Cell Achieved Through Control of Carrier Recombination in Nanostructures. *Nat. Nanotechnol.* **2012**, *7*, 743−748.
(47) Liardet, L.; Katz, J. E.; Luo, J.; Grätzel, M.; Hu, X. An Ultrathin Cobalt−Iron Oxide Catalyst for Water Oxidation on Nanostructured Hematite Photoanodes. *J. Mater. Chem. A* **2019**, *7*, 6012−6020.
(48) Young, J. L.; Steiner, M. A.; Döscher, H.; France, R. M.; Turner, J. A.; Deutsch, T. G. Direct Solar-to-Hydrogen Conversion via Inverted Metamorphic Multi-Junction Semiconductor Architectures. *Nat. Energy* **2017**, *2*, No. 17028.
(49) Cheng, W.-H.; Richter, M. H.; May, M. M.; Ohlmann, J.; Lackner, D.; Dimroth, F.; Hannappel, T.; Atwater, H. A.; Lewerenz, H. J. Monolithic Photoelectrochemical Device for Direct Water Splitting with 19% Efficiency. *ACS Energy Lett.* **2018**, *3*, 1795−1800.

https://doi.org/10.1021/acs.jpcc.1c10148
J. Phys. Chem. C 2022, 126, 5970−5979